Journal of Magnetic Resonance 305 (2019) 138–145

Contents lists available at ScienceDirect

Journal of Magnetic Resonance

journal homepage: www.elsevier.com/locate/jmr

Dynamic nuclear polarisation of liquids at one microtesla using circularly polarised RF with application to millimetre resolution MRI

Ingo Hilschenz [a], Sangwon Oh [a], Seong-Joo Lee [a], Kwon Kyu Yu [a], Seong-min Hwang [a,b], Kiwoong Kim [a,b], Jeong Hyun Shim [a,b,*]

[a] Korean Research Institute of Standards and Science, Daejeon 34113, Republic of Korea
[b] Department of Medical Physics, University of Science and Technology, Daejeon 34113, Republic of Korea

ARTICLE INFO

Article history:
Received 9 April 2019
Revised 18 June 2019
Accepted 24 June 2019
Available online 29 June 2019

Keywords:
MRI
Low field
Ultra low field
Dynamic nuclear polarization
Overhauser
Nitroxide radical

ABSTRACT

Magnetic resonance imaging in ultra-low fields is often limited by mediocre signal-to-noise ratio hindering a higher resolution. Overhauser dynamic nuclear polarisation (O-DNP) using nitroxide radicals has been an efficient solution for enhancing the thermal nuclear polarisation. However, the concurrence of positive and negative polarisation enhancements arises in ultra-low fields resulting in a significantly reduced net enhancement, making O-DNP far less attractive. Here, we address this issue by applying circularly polarised RF. O-DNP with circularly polarised RF renders a considerably improved enhancement factor of around 150,000 at 1.2 μT. A birdcage coil was adopted into an ultra-low field MRI system to generate the circularly polarised RF field homogeneously over a large volume. We acquired an MR image of a nitroxide radical solution with an average in-plane resolution of 1 mm. De-noising through compressive sensing further improved the image quality.

© 2019 Elsevier Inc. All rights reserved.

1. Introduction

Nuclear magnetic resonance (NMR) at ultra-low fields has attained interest in several fields such as combining magnetic resonance imaging (MRI) with magnetoencephaolography (MEG) [1,2], resolving *J*-coupling structures in molecules [3–5], enhancing MRI contrast between certain biological tissues [6], obtaining MR image of samples enclosed in metal [7], detecting neuronal currents directly [8,9] and measuring fundamental quantities [10]. The detection of NMR signals in ultra-low fields, typically below the earth's magnetic field, requires highly sensitive sensors, such as superconducting quantum interference devices (SQUID) [11,12] or optically-pumped atomic magnetometers [13,14]. However, the thermal nuclear polarisation in ultra-low fields is not sufficiently large. Thus, most implementations of ultra-low field NMR/MRI temporally increase the magnetic field above tens of millitesla through a process known as pre-polarisation. This has been conducted using either *in situ* electromagnets or *ex situ* permanent magnets. Strong pre-polarisation fields produced by electromagnets entail inducing eddy currents in the shielding walls and magnetise the superconducting pick-up coils, which may interfere with the detection of weak NMR signals [15–18]. *Ex situ* pre-polarisation requires the pneumatic shuttling of a sample from a remote location to the detection space. The shuttling can be an obstacle for reliable repetitions required in two-dimensional spectroscopy or MRI.

Inducing hyperpolarised states in the target samples has been an alternative approach [19–23]. In Overhauser dynamic nuclear polarisation (O-DNP), the polarisation of electron spins belonging to free radicals is transferred to that of nuclear spins of the target molecules in a solution[24]. However, O-DNP has hardly been used at a magnetic field range below a few millitesla [20,25–27], because its effectiveness at enhancing the thermal polarisation significantly degrades in ultra-low fields. When applying the RF for O-DNP, positive and negative enhancements occur simultaneously, and in turn cancel each other out [19,28].

Nevertheless, Lee et al. [29] adopted O-DNP for MRI in a magnetic field of 34.5 μT, unfortunately the image resolution was not satisfactory owing to the low enhancement of the thermal polarisation. In this study, we address this issue by using circularly polarised RF fields, which selectively induces either positive or negative enhancements. The thermal nuclear polarisation was increased by a factor of 150,000 at 1.2 μT, overcoming the Overhauser limit. An Overhauser-enhanced MRI of a nitroxide radical solution with circularly polarised RF rendered a decent signal-to-noise ratio and allowed us to strengthen the field gradients for improving the image resolution. A birdcage coil, widely used in high-field MRI, serves as a transmitting coil for generating a circularly polarised RF with a satisfactory spatial uniformity. In addition, a compressed sensing technique was applied to de-noise the

* Corresponding author.
E-mail address: jhshim@kriss.re.kr (J.H. Shim).

https://doi.org/10.1016/j.jmr.2019.06.013
1090-7807/© 2019 Elsevier Inc. All rights reserved.

obtained images. This work demonstrates that higher image resolution can be obtained using O-DNP with circular polarised RF fields in combination with nitroxide radicals at the microtesla scale, without the aid of a strong pre-polarisation fields or shuttling.

2. Theoretical model

To explain O-DNP in ultralow fields, we formulate a model and thereby express the enhancement factor in a more intuitive form, by neglecting the effects of a magnetic field when necessary.

2.1. Spin Hamiltonian

In the presence of a magnetic field $\boldsymbol{B}$, the Hamiltonian of a nitroxide radical can be expressed as $\mathcal{H} = A\boldsymbol{S}\cdot\boldsymbol{I} - (\gamma_e\boldsymbol{S} + \gamma_n\boldsymbol{I})\cdot\boldsymbol{B}$, in which $\boldsymbol{S}$ and $\boldsymbol{I}$ are electron ($S = 1/2$) and ^{14}N nuclear ($I = 1$) spins. The gyromagnetic ratios of the electron and nuclear spins are labelled as γ_e and γ_n, respectively. In ultra-low fields, the hyperfine coupling A between electron and ^{14}N spins in the radical is dominant over the Zeeman energies, making $\boldsymbol{S}$ and $\boldsymbol{I}$ strongly coupled. To diagonalise the Hamiltonian, the basis states $|F, m_F\rangle$ of spin $\boldsymbol{F} = \boldsymbol{S} + \boldsymbol{I}$ are required. The Hamiltonian transforms into

$$\mathcal{H} = A\frac{F(F+1)}{2} - \gamma_F(F)\boldsymbol{F}\cdot\boldsymbol{B} + C. \tag{1}$$

The first term represents the zero field splitting (ZFS) of $3A/2$ between the quartet of $F = 3/2$ and the doublet of $F = 1/2$ in the energy diagram (Fig. 1(a)). The second term is the Zeeman energy of the spin $\boldsymbol{F}$, and the last a constant independent of F. The exact expression of the gyromagnetic ratio $\gamma_F(F)$ is given as,

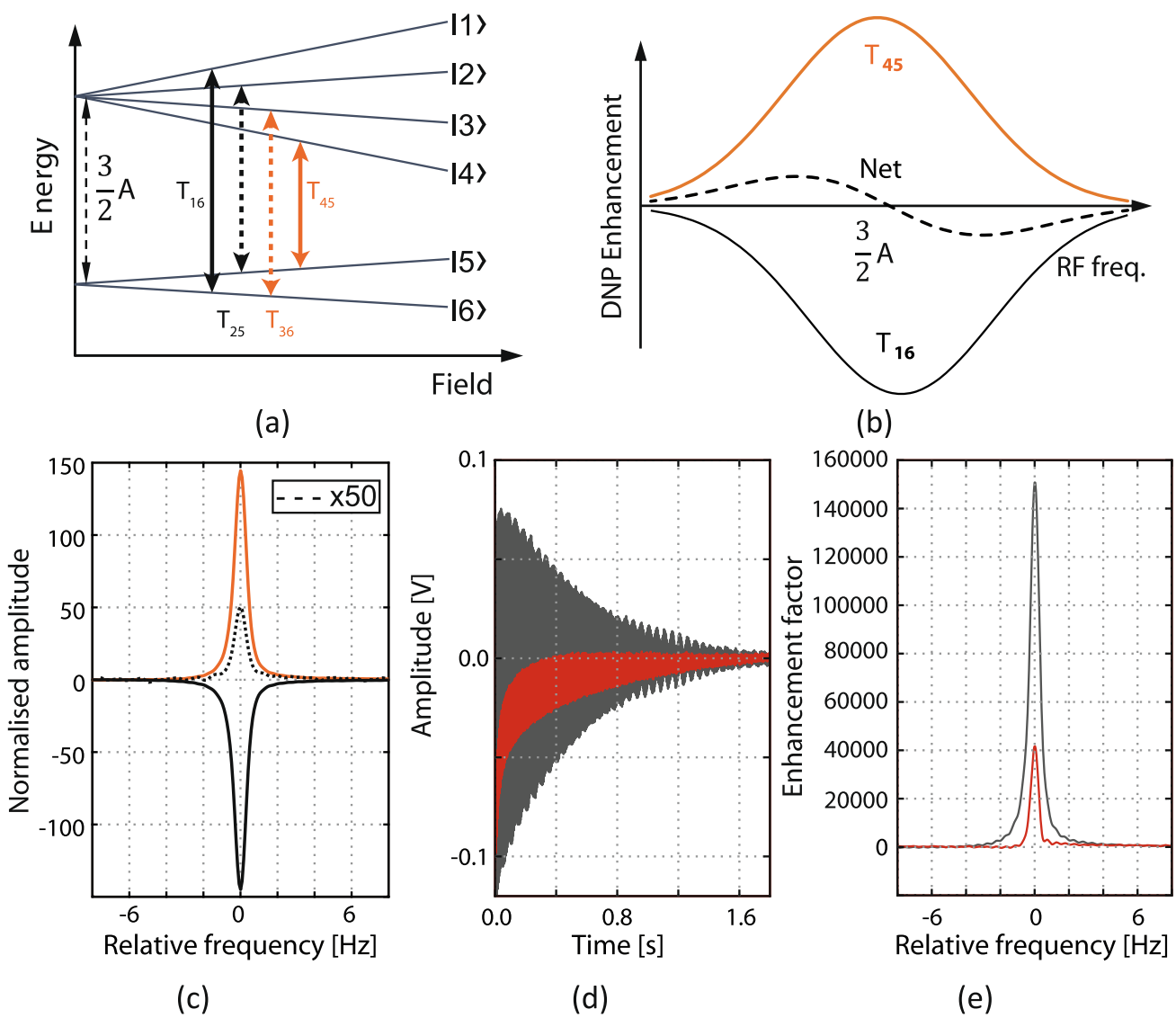

Fig. 1. (a) Energy levels of nitroxide radicals in ultra-low fields plotted as a function of the magnetic field. The allowed transitions when the magnetic field and oscillating RF field are orthogonal, are illustrated as arrows. (b) A schematic of the Overhauser-enhanced nuclear polarisations for T_{45} and T_{16}. Owing to the concurrence of positive (orange) and negative (black) enhancements, the net (dashed) is significantly reduced. T_{25} and T_{36} have negligible contributions to the net enhancement (see the text). (c) NMR spectra with a polarising field of B_p 1.2 μT enhanced using O-DNP with circular polarisation $\phi = 90^\circ$ (orange), $\phi = 270^\circ$ (black). The vertical scale is normalised to the linearly polarised signal (dashed line). The RF frequency of the linear polarisation was 69 MHz which is near the maximum of the net curve in (b) [19] corresponding to what can be achieved with applying a circular polarising field. (d) NMR signals obtained with O-DNP using circularly polarised RF (gray) and a pre-polarisation field of 50 mT (red), and (e) their spectra scaled to the enhancement in comparison with the thermal nuclear polarisation at 1.2 μT. (For interpretation of the references to colour in this figure legend, the reader is referred to the web version of this article.)

$$\gamma_F(F) = \frac{\gamma_e}{2}\left[1 + \frac{S(S+1) - I(I+1)}{F(F+1)}\right] + \frac{\gamma_n}{2}\left[1 - \frac{S(S+1) - I(I+1)}{F(F+1)}\right]. \quad (2)$$

We can approximate $\gamma_F(3/2) = \gamma_e/3$ and $\gamma_F(1/2) = -\gamma_e/3$ as $|\gamma_e|$ is nearly 10^4 times larger than γ_n ($\frac{\gamma_e}{2\pi}$ = −28 GHz/T, $\frac{\gamma_n}{2\pi}$ = 3.077 MHz/T for ^{14}N). The eigenstates depicted in Fig. 1(a) are $|1\rangle = |3/2, 3/2\rangle$, $|2\rangle = |3/2, 1/2\rangle$, $|3\rangle = |3/2, -1/2\rangle$, $|4\rangle = |3/2, -3/2\rangle$, $|5\rangle = |1/2, -1/2\rangle$ and $|6\rangle = |1/2, 1/2\rangle$.

2.2. Enhancement factor

When an oscillating field $\boldsymbol{B}(t)$ is applied, the transitions between the states can be induced. The polarising field B_p is perpendicular to $\boldsymbol{B}(t) = B_{RF}[\cos(\omega t)\hat{x} + \cos(\omega t + \phi)\hat{z}]$. Thus, T_{16}, T_{25}, T_{36} and T_{45}, shown as arrows in Fig. 1 (a), are the allowed transitions under the selection rule $\Delta m_F = \pm 1$ and have non-negligible frequencies across ZFS. At one microtesla, the difference between the transition frequencies and ZFS is in the order of $|\gamma_F B| \simeq 10$ kHz, which is insignificant compared to ZFS. Therefore, the four transitions occur simultaneously when exposed to an RF frequency of ZFS (72 MHz). Given the saturation of a transition T_{ij}, the DNP enhancement factor is proportional to the variation of the spin moment $\Delta\langle\gamma_F(F)\boldsymbol{F}_z\rangle_{ij}$. Thus, the formula for the enhancement factor ε in Ref. [28] can be applied to the spin $\boldsymbol{F}$ as,

$$\varepsilon_{ij} = \rho f s \frac{\Delta\langle\gamma_F(F)\boldsymbol{F}_z\rangle_{ij}}{|\gamma_F(F)|I_0}, \quad (3)$$

in which I_0 is the proton spin polarisation in thermal equilibrium. (ρ, f, and s are coupling constant, leakage factor, and saturation factor.)

According to the calculation (see the Appendix B), the max enhancement for a transition T_{ij} can be obtained as

$$\varepsilon_{ij}^{max} = -\frac{A}{4\gamma_I B}\frac{m_F^i + m_F^j}{2}, \quad (4)$$

where m_F^i represents m_F of the state $|i\rangle$. Thus, T_{25} and T_{36} do not exhibit significant enhancements, whereas T_{16} and T_{45} do, although with opposing signs. This leads to the concurrence of positive and negative enhancements, cancelling each other out. The net enhancement is significantly lower, when applying a linear polarised RF field, than the individual enhancements, as shown in Fig. 1 (b). Applying circularly polarised RF fields can help address this issue by selectively inducing either $T_{16}(\Delta m_F = +1)$ or $T_{45}(\Delta m_F = -1)$.

3. Results

3.1. O-DNP enhancement with circularly polarised RF

Fig. 1(c) discloses that, O-DNP with circularly polarised RF renders a considerably increased enhancement, over 140-fold. The dashed line corresponds to a data set acquired with linearly polarised RF, whereas the orange and black lines represent circularly polarised RF. The polarity of the O-DNP enhancement is solely determined based on the relative phase ϕ of the quadrature RF field (the orange ($\phi = 90°$) and black ($\phi = 270°$) lines in Fig. 1(c)), which is what the theoretical model predicts.

In order to estimate how much O-DNP can enhance the thermal nuclear polarisation with a circularly polarised RF, at a polarising field of 1.2 μT, we instead applied a pre-polarisation field B_p of 50 mT for comparison. Fig. 1(d) illustrates that the higher polarising field increases the eddy currents, resulting in a notable dc-drift in the initial time after the pre-polarisation field has turned off (please compare the red and black curve). The Overhauser-enhanced NMR signal was found out to be 3.6 times as high as that obtained with the pre-polarisation field (Fig. 1(d) and (e)). Thus, utilising O-DNP with circularly polarised RF, is equivalent to applying a pre-polarisation field of 180 mT, indicating the total enhancement factor can be estimated to around 150,000. The enhancement factor of the linearly polarised RF shown in Fig. 1(b) is around 1030 at 1.2 μT.

The degree of the enhancement with circularly polarised RF is far higher than what the conventional theory of O-DNP states when the Zeeman energy is dominant over the hyperfine coupling. According to it, the enhancement factor is limited to the ratio of gyromagnetic constants as $\frac{\gamma_S}{\gamma_I}$, which leads to only 660 for proton spins [24]. According to Eq. (4), the enhancement factor can reach up to 235,000 at 1.2 μT, which is certainly consistent with our result. Zero field splitting plays a crucial role for such a high enhancement factor. Due to its presence, the population difference between the upper quartet and lower doublet in Fig. 1(a) becomes independent of the magnetic field and proportional to ZFS as $\frac{3A}{2k_BT}$ (Eq. (B.3)), making the enhancement of the thermal nuclear polarisation scales as $\frac{A}{4\gamma_I B}$ (Eq. (4)). This elucidates how the enhancement beyond the Overhauser limit was accomplished and can be even higher at a lower magnetic field.

3.2. Overhauser-enhanced MRI

Overhauser-enhanced imaging was conducted using our ultra-low field MRI system (Fig. 2(a)). The MR sequence is based on a spin-echo measurement (Fig. 2 (b)) where we used a polarisation time t_{pol} of 2000 ms, a phase encoding time t_{ph} of 100 ms, a read-out time t_{acq} of 200 ms and a delay time t_d between measurements of 1000 ms. The frequency encoding gradient (FEG) G_z strength was 229.8 $\frac{\mu T}{m}$, and the phase encoding gradient (PEG) G_x was 186.0 $\frac{\mu T}{m}$ at a maximum of 141 steps in- between. The total acquisition time constituted to 77 min. The phantom in the present work is the same as in our previous study [29] and was filled with a 2 mM TEMPOL (4-hydroxy-2,2,6,6-tetramethylpiperidin-1-oxyl) solution which seemed to achieve the optimal result in the microtesla field range[30,31]. It has the dimensions of 54 mm ∗ 43.5 mm ∗ 40 mm, featuring a letter K in the middle as well as rectangles and circles with varying sizes (top 10 mm, middle 5 mm, bottom 3 mm) on the left and right sides, respectively. For O-DNP, we applied a polarising field B_p of 1.2 μT. The imaging field B_m is 20.69 μT, corresponding to a Larmor frequency of 880 Hz.

The obtained image with a sub-millimetre voxel size (in the 2D plane) of 0.76 mm ∗ 0.56 mm, is shown in Fig. 3(a). The image shows distortion owing to the presence of concomitant gradients [32] and inhomogeneity in the signal strength. The latter is caused by the spatial inhomogeneity in the sensitivity of the pick-up coil, as discussed in Ref. [19], and the off-resonance effect of the refocusing B_1 pulse (see the discussion).

3.3. De-noising using compressive sensing

To further improve the image quality, we applied compressive sensing (CS) for de-noising. Unlike filtering the image in the k-space, which increases the SNR at the expense of the spatial resolution, CS can de-noise the data without a loss of image resolution, although at the cost of computation time. We adapted the conjugate gradients method to solve the unconstrained optimisation problem [33]. The equation for convex optimisation can be written

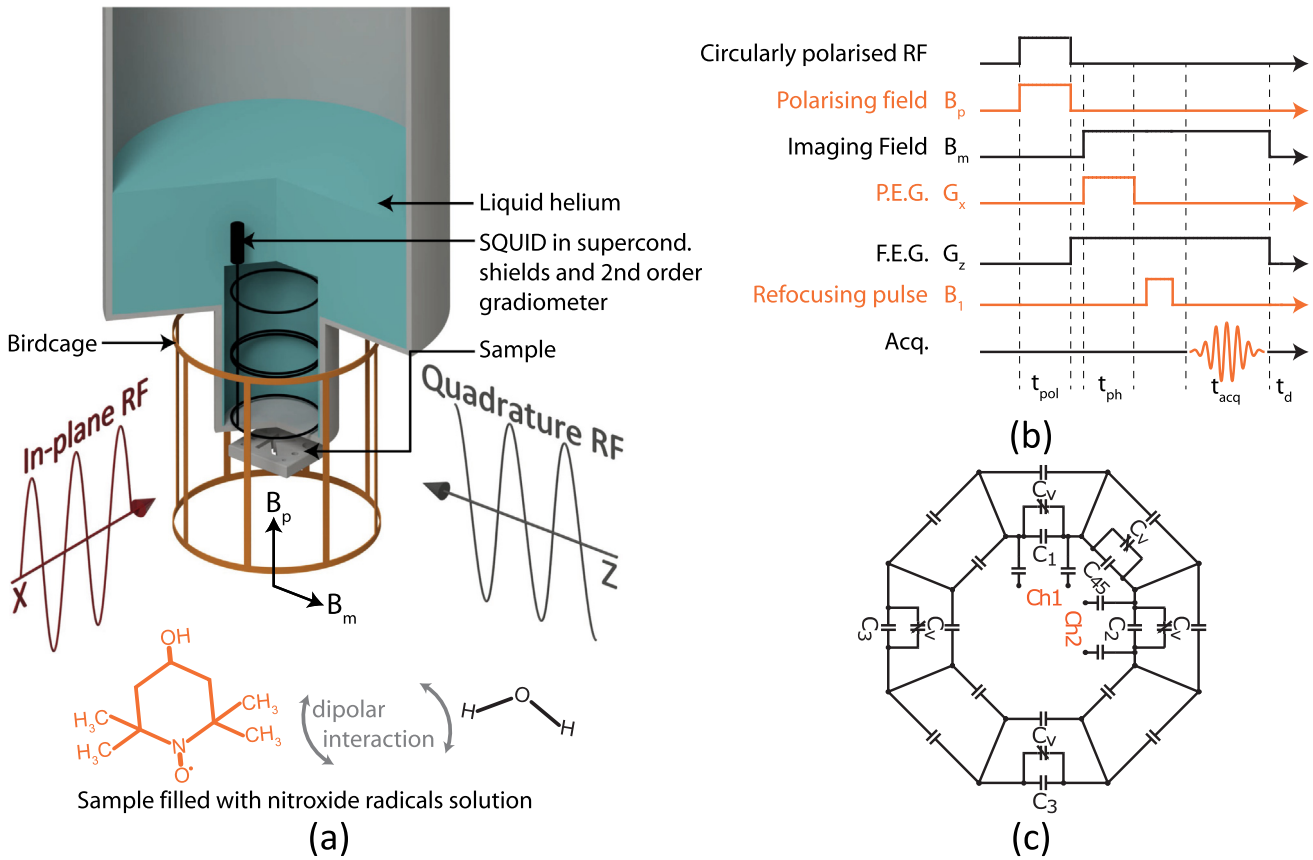

Fig. 2. (a) Schematic of the ultra-low field MRI system, including the SQUID sensor, birdcage RF coil, and phantom that contains a nitroxide radical (TEMPOL) solution. (b) Timing sequence generating the spin-echo signals, with a refocusing B_1 pulse. Prior to this, the polarising field B_{pol} and circularly polarised RF are applied simultaneously for O-DNP. Phase-encoding (PEG) and frequency- encoding gradient fields (FEG) are coding the 2D image. We used a polarisation time t_{pol} of 2000 ms, a phase encoding time t_{ph} of 100 ms, and a read-out time t_{acq} of 200 ms and the delay t_d between consecutive measurements is 1000 ms. (c) Circuit schematic of the high-pass birdcage coil, the capacitor values of which are all approximately 50 pF, and the trimmer capacitors range is C_V = (1–12) pF.

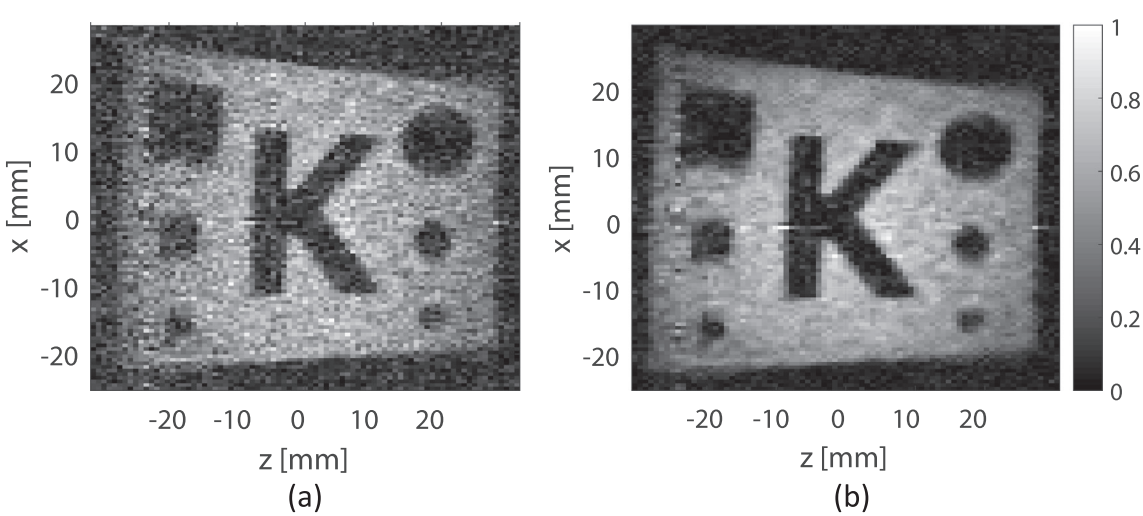

Fig. 3. Images of our phantom obtained at a voxel size of 0.76 mm ∗ 0.54 mm in the z- and x-directions: (a) unprocessed image, and (b) image from the same data set but treated using a compressed sensing method.

as $Ł = argmin\{||Fm - y||_2^2 + \lambda||Wm||_1\}$, where F and W denote fast Fourier and wavelet transformations, respectively; m is a solution with the reconstructed image in real space; y is an input, which is the k-space image data. λ is a weighting factor for the sparsity, and its value was optimised after several verification runs.

A contrast enhancement and a better image quality can be observed after CS treatment of the image (Fig. 3(b)). In addition, the standard deviation of the background noise has been significantly reduced, which leads to a perceivable improvement in the SNR of the image.

4. Discussion

4.1. Image resolution

To estimate the spatial resolution (z-direction) of the image shown in Fig. 3(a) we fitted the data slices across the edges of the letter K in the image with a Fermi function. From the first derivative of the fit function, we can then obtain the image resolution, which is represented as the full width at half maximum (see the supplementary information). The average resolution obtained with this method was 1.05 mm. The lower resolution compared to the voxel size may stem from the partial volume effect induced by the inhomogeneous field gradient. We found that the background field varies from 50 to 200 nT over the sample space in our magnetically shielded room. Demagnetising the μ-metal layers used in the surrounding walls of the magnetically shielded room will alleviate the residual field gradient. We also investigated a Larmor frequency drift, but it only accounts for less than a 0.1 mm image shift over the 77 min measurement period.

4.2. Off-resonance effect

In the sequence shown in Fig. 2(b), the frequency encoding gradient G_z turns on immediately after the O-DNP process, and is not turned off, even while a refocusing B_1 pulse is applied. This simplifies the entire sequence; however, if the B_1 strength is weaker than the field generated by the gradient coil, a strong off-resonance effect occurs. This causes a reduction of the spin echo signal strength. We irradiated a strong B_1 pulse, which is estimated to be over 20 μT from the nutation curve. Because it is circularly polarised, the B_1 field does not induce the Bloch-Siegert effect [34]. However, the off-resonance effect is not negligible, as the gradient field increases along the z-axis. Thus, the flip-angle of the B_1 pulse eventually deviates from 180°, reducing the spin echo intensity. The calculation of the transverse component of the magnetisation after the refocusing B_1 pulse in the presence of the off-resonance field revealed that the spin echo signal gradually decreases along the z-axis and reduces to 90% at the edges of the phantom (see the supplementary information).

4.3. Imaging time

The total elapsed time of 77 min for the image in Fig. 3(a) seems not promising. However, 90% of the measurement time is consumed by the polarisation time and the delay between measurements. There remain several methods for achieving a faster image acquisition. A rapid acquisition with relaxation enhancement (RARE) [35] sequence can be used to accelerate the experiment to a large extent, by taking advantage of filling multiple k-space lines at the T_2 time scale within a single shot, thereby shortening the acquisition time. Here, T_2 is nearly comparable with T_1 in liquid phases, and the polarisation time used in this study is close to the value of T_1 in the TEMPOL solution. Therefore, a RARE sequence is applicable. A time saving of at last 50% should be possible, which may be further increased if we reduce our phase encoding time and increase the gradient fields for compensation. In addition, the delay between measurements could be further reduced if the magnetically shielded room has been optimised for eddy current suppression, such as reducing the size of the conductive plates used for RF shielding [17].

4.4. RF exposure to He dewar

One side effect of applying O-DNP uncovered during the present study is the increase in the boil-off rate of the liquid helium stored in the dewar. Because the bottom of the dewar is located inside the birdcage coil, the superinsulation layers on the inside of the dewar are exposed to RF radiation, which causes RF absorption as the sequence runs. Placing additional RF shielding layers at the outmost surface of the dewar is expected to mitigate this issue.

5. Conclusion

It has been widely accepted that O-DNP with nitroxide radicals requires a magnetic field higher than hundreds of microtesla for optimal efficiency [28]. However, we demonstrated that circularly polarised RF results in a substantially higher enhancement factor of over 150,000 at 1.2 μT and can be implemented with a birdcage coil. The magnetic field applied for O-DNP was only 1.2 μT (B_p), which is approximately 30 times lower than 34.5 μT in our previous work [29]. However, the quality of the image (Fig. 3(a)) exhibits an appreciable improvement. We expect this method to broaden the scope of Overhauser-enhanced MRI in ultra-low fields or even near zero fields. Because the magnetic field used in this work for O-DNP is no higher than a few microtesla, optically-pumped atomic magnetometers [13] can be adopted in direct detection of the NMR signal as in Ref. [36], with a more suppressed transient ^{87}Rb oscillation and yet a higher nuclear polarisation. This leads to a potentially non-cryogenic ultra-low field MRI system capable of a reasonable resolution.

Acknowledgement

This work was supported by the Development of Core Technology for Advanced Scientific Instrument (KRISS2019GP2019-0018) and the Development of Platform Technology for Innovative Medical Measurements Program (KRISS-2019-GP2019-0013) from the Korea Research Institute of Standards and Science. We would like to thank Yeunchul Ryu's group at the Neuroimaging Research Center of Gachon University, for the initial help and advice on building the birdcage coil.

Appendix A. Gyromagnetic ratio of the spin *F*

The calculation of the gyromagnetic ratio of the spin $\boldsymbol{F}$ can be done similarly to that for Lande-g factor. We assume that $\gamma_F(F)$ satisfies the equation below,

$$\gamma_e \boldsymbol{S} + \gamma_n \boldsymbol{I} = \gamma_F(F)\boldsymbol{F}. \tag{A.1}$$

On both sides of the Eq. (A.1), we do the inner product of the spin $\boldsymbol{F}$, and replace $\boldsymbol{S}\cdot\boldsymbol{I}$ by $\frac{1}{2}[\boldsymbol{F}^2 - (\boldsymbol{S}^2 + \boldsymbol{I}^2)]$. Then, the equation below can be obtained:

$$\frac{\gamma_e}{2}[\boldsymbol{F}^2 + (\boldsymbol{S}^2 + \boldsymbol{I}^2)] + \frac{\gamma_n}{2}[\boldsymbol{F}^2 - (\boldsymbol{S}^2 + \boldsymbol{I}^2)] = \gamma_F(F)\boldsymbol{F}^2. \tag{A.2}$$

$|F, m_F\rangle$ are linear superposition states of the product of individual spin states as $|F, m_F\rangle = \sum_{m_S, m_I} c_{m_S, m_I} |S, m_S\rangle |I, m_I\rangle$. Thus, the equations $\langle \boldsymbol{F}^2\rangle = F(F+1), \langle \boldsymbol{S}^2\rangle = S(S+1)$, and $\langle \boldsymbol{I}^2\rangle = I(I+1)$ can be applied to the expectation values of both sides of the Eq. (A.2). Then, we can obtain Eq. (2).

Appendix B. Calculation of the enhancement factor

According to the Eq. (3), the enhancement factor is proportional to the deviations of the radical's magnetic moment from its thermal equilibrium under a resonant oscillating field. When a transition T_{ij} is induced, the deviation of the magnetic moment of the spin $\boldsymbol{F}_z$ is defined as,

$$\Delta\langle \gamma_F(F)\boldsymbol{F}_z\rangle_{ij} = \gamma_F(F) m_F^i \Delta n_i + \gamma_F(F) m_F^j \Delta n_j, \tag{B.1}$$

in which $\Delta n_k = n_k - n_k^{eq}$ is the population change of the state $|k\rangle$, as shown in Fig. 1(a). Populations at thermal equilibrium are determined by Boltzmann's law as $n_k^{eq} = \exp(-\frac{E_k}{k_B T})/Z$. ($Z = \sum_k \exp(-\frac{E_k}{k_B T})$). In ultralow fields, ZFS is significantly larger than Zeeman energies. Therefore, it is reasonable to assume that, at thermal equilibrium, the states in the quartet have the same population as $n_1^{eq} = n_2^{eq} = n_3^{eq} = n_4^{eq} = n(\frac{3}{2})$, and so do the states in the doublet as $n_5^{eq} = n_6^{eq} = n(\frac{1}{2})$. $n(\frac{3}{2})$ and $n(\frac{1}{2})$ satisfy the relation,

$$n\left(\frac{3}{2}\right)/n\left(\frac{1}{2}\right) = \exp\left(-\frac{3A}{2k_B T}\right). \tag{B.2}$$

With the condition that $\sum_k n_k = 1$ and high temperature approximation, the population difference between the doublet and quartet is,

$$\delta n = n\left(\frac{1}{2}\right) - n\left(\frac{3}{2}\right) = \frac{A}{4k_B T}. \tag{B.3}$$

If a transition T_{ij} ($i \in \{1,2,3,4\}, j \in \{5,6\}$) is fully saturated, the population of n_i and n_j will be equal to their average $\frac{1}{2}\left[n(\frac{3}{2}) + n(\frac{1}{2})\right]$. Thus, $\Delta n_i = \frac{1}{2}\left[-n(\frac{3}{2}) + n(\frac{1}{2})\right] = \frac{\delta n}{2}$ and $\Delta n_j = \frac{1}{2}\left[n(\frac{3}{2}) - n(\frac{1}{2})\right] = -\frac{\delta n}{2}$. By putting these into Eq. (B.1), we can derive the approximate equation below,

$$\Delta\langle\gamma_F(F)\boldsymbol{F}_z\rangle_{ij} = \frac{1}{6}\gamma_e \delta n(m_F^i + m_F^j). \tag{B.4}$$

In order to estimate the maximal theoretical enhancement, we assume $s = 1$ and $f = 1$ in Eq. (3). When the dipolar interaction is dominant in Overhauser DNP, the coupling factor ρ becomes positive ($\rho = 0.5$). With the thermal nuclear polarisation $I_0 = \frac{\gamma_I B}{2k_B T}$ and Eq. (B.4), the maximal enhancement can be derived as

$$\varepsilon_{ij}^{max} = -\frac{A}{4\gamma_I B}\frac{m_F^i + m_F^j}{2}. \tag{B.5}$$

Therefore, the saturation of T_{16} ($m_F^1 + m_F^6 = 2$) induces negative enhancement, while T_{45} ($m_F^4 + m_F^5 = -2$) positive as illustrated in Fig. 1(b).

Appendix C. Experimental methods

C.1. Ultra-low field MRI system

A schematic of the experimental setup used for our ultra-low field imaging system is shown in Fig. C.1. The coils, sensor system, and sample are located inside a magnetically shielded room. Our low noise Helium dewar contains a direct current SQUID (Supracon AG) to which a second-order gradiometer with a baselength of 50 mm and a diameter of 65 mm is connected. It is made of a Niobium wire with a diameter of 125 µm and oriented along the y-direction. The SQUID is shielded with two superconducting layers. The sensor itself has a noise level of approximately 3 fT·Hz$^{-\frac{1}{2}}$. With all magnetic fields, required for the measurement activated, the noise level increases to 5 fT·Hz$^{-\frac{1}{2}}$. The main contributors are the frequency encoding gradient field G_z and the imaging field B_m.

The imaging coils include gradient coils in all three main directions G_x, G_y, and G_z, as well as the imaging field B_m along the z-direction. All coils are wound on a wooden frame, which was carefully manufactured to avoid magnetic impurities. We also tried to avoid the use of magnetic materials wherever possible. The coil system consist of two frames, each separated by approximately 0.66 m, with an edge length of 1.375 m. The G_x gradient coil is used for the phase encoding, whereas G_z is used for the frequency encoding. Helmholtz coils along the x- and y-directions are utilised to generate a circular polarised B_1 pulse [34]. An additional coil along the y-direction provides a weak polarising field B_{pol} of 1.2 µT. These coils are wound on a wooden cube structure, which supports the sensor system. The imaging field B_m is 20.69 µT, corresponding to a Larmor frequency of 880 Hz.

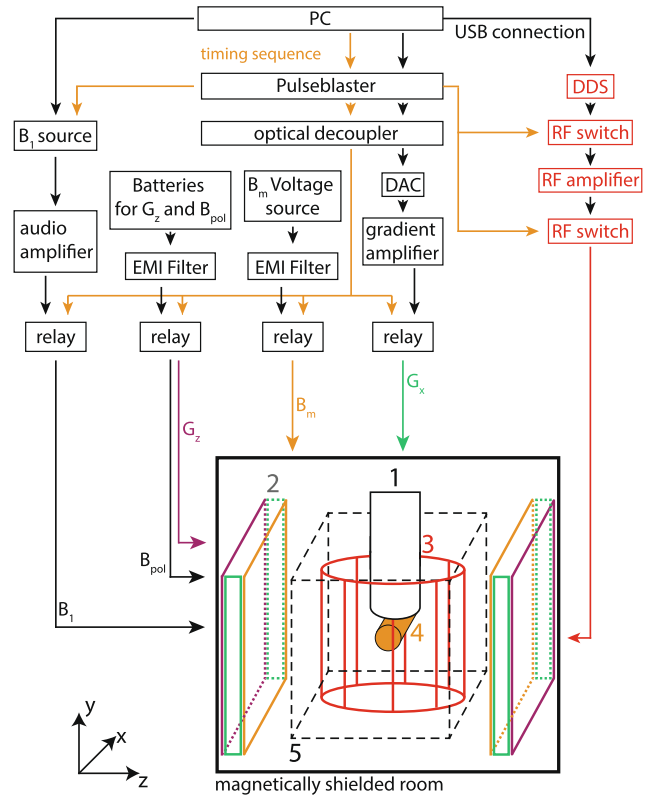

Fig. C.1. A schematic of the ultra-low field MRI system is shown, including SQUID sensor system (1), gradient (PEG G_x, and FEG G_z) and imaging field B_m coils (2), birdcage coil (3), sample (4), the tipping coil B_1 in x- and y-direction and B_p coil for a polarisation field along the y-direction (5).

The necessary digital triggers are generated using a timing signal generator (PulseBlaster, Spincore), and fed to an optical decoupler array. The relay switches are then addressed using optical fibres. They are required to decouple the coils from the current sources, while the signal acquisition runs, reducing the noise level. We used batteries for the relatively weak polarising field B_{pol} and the frequency encoding gradient G_z to reduce the power-line noise. The imaging field B_m is generated using a low noise current source (Keithley PWS4323) for stability.

To generate a circularly polarised B_1 pulse, we used a two-channel frequency generator (Agilent 33500B) programmed for arbitrary waveforms for accurate pulse shapes. Both channels apply a signal with a frequency corresponding to a Larmor frequency of 880 Hz. The outputs were then amplified using a two-channel audio amplifier and fed through relays, which decouples the signals during the acquisition time. We attached a very detailed schematic of the experimental setup in the supplementary information for the interested readers.

C.2. Imaging sequence

A spin-echo sequence was used for imaging, as shown in Fig. 2 (c). Unlike a conventional sequence, the initial tipping pulse is omitted because B_p, along which the enhanced nuclear magnetisation aligns, is orthogonal to B_m. Thus, only a refocusing pulse is necessary for a spin echo. We use a polarisation time t_{pol} of 2000 ms, a phase encoding time $t_p h$ of 100 ms, and a read-out time t_{acq} of

200 ms. The echo time is approximately 200 ms, which is much shorter than the T_2 time of the sample. The resulting signal loss is approximately 10%. The duration for the B_1 pulse is 0.58 ms. To suppress the effects of eddy currents induced in the walls of the magnetically shielded room, we applied an additional delay of 1000 ms (t_d) between each measurement, which is relatively long because the shielding walls of the magnetically shielded room are not optimised for suppressing the eddy current effects and last a fairly long time.

C.3. Circularly polarised RF

Because hyperfine coupling (A) between the electron and ^{14}N nuclear spins is approximately 48 MHz, zero-field splitting ($= 3A/2$) occurs at near 72 MHz [19], which is the frequency of the circularly polarised RF field used. Two phase-synced sinusoidal waves are generated using an in-house built direct digital synthesizer (DDS, AD9958). The phase shift between them is adjusted for circular polarisation. The in-phase and quadrature RF signals are amplified separately up to 18 W. We monitor the amplified RF signals using two directional couplers (Pulsar C30-102-481/2N) to confirm the power and phase consistency. High-power RF switches positioned after the amplifier reduce the disturbances of the SQUID sensor during data acquisition. The amplified RF signals, in-phase and quadrature, are fed to the birdcage coil inputs.

C.4. Birdcage coil

A single birdcage coil can generate circularly polarised RF fields by driving the coil with in-phase and quadrature RF signals aligned perpendicularly. It is more suitable than a quadrature surface coil owing to its high spatial homogeneity in the coil volume and ease of access. Among the three types of birdcage coils, we have chosen the high-pass type. The coil consists of legs, also referred to as rungs, which are equally spaced around the surface of the cylinder. They connect to one ring on either end of the cylinder. For the high-pass type, the capacitors are located on the ring, between the segments of the end points of the rungs. We used 5 mm wide, thin circuit board strips to build the coil, allowing it to be sufficiently flexible to follow the curvature of the cylinder body. The input circuit is balanced, using two matching capacitors C_m.

To suppress common mode currents through the coax cables connected to the input circuits, we added cable traps tuned to 72 MHz at every half-wavelength position. A magnetic field probe [37] was built for the tuning of the cable traps. Additionally, ferrite cores were positioned at the end of the coax cables connected to the RF amplifier. The developed birdcage coil electrical schematic is shown in Fig. 2(c). The coil has an outer diameter of 15 cm with eight legs, each 15 cm long. We chose a ratio close to 1:1 for diameter-to-rung lengths to maximise the homogeneity of our coil [38]. The "Birdcage Builder" software was used to calculate the required capacitance [39]. Adjustments of all capacitors for tuning and matching were applied with the dewar reaching inside the birdcage coil, because metallic components in the dewar strongly disturb the resonance modes. Fine adjustments prior to each measurement can be conducted using the variable capacitors (Voltronics V9000). If one disregards the end ring modes, the main mode has the highest frequency [40–42].

The crosstalk was adjusted using C_{45}, which defines the independence of the two input channels. If the two channels have a higher crosstalk, the resulting field will converge to a linear polarised field rather than the intended circular polarised field. We achieved a crosstalk of 13% in amplitude, which was measured by placing a pick-up coil at the centre of the birdcage coil and rotating it.

Appendix D. Supplementary material

Supplementary data associated with this article can be found, in the online version, at https://doi.org/10.1016/j.jmr.2019.06.013.

References

[1] P. Volegov, A.N. Matlachov, M.A. Espy, J.S. George, R.H. Kraus, Simultaneous magnetoencephalography and squid detected nuclear mr in microtesla magnetic fields, Magn. Reson. Med. 52 (3) (2004) 467–470.
[2] P.T. Vesanen, J.O. Nieminen, K.C. Zevenhoven, J. Dabek, L.T. Parkkonen, A.V. Zhdanov, J. Luomahaara, J. Hassel, J. Penttilä, J. Simola, et al., Hybrid ultra-low-field mri and magnetoencephalography system based on a commercial whole-head neuromagnetometer, Magn. Reson. Med. 69 (6) (2013) 1795–1804.
[3] R. McDermott, A.H. Trabesinger, M. Mck, E.L. Hahn, A. Pines, J. Clarke, Liquid-state nmr and scalar couplings in microtesla magnetic fields, Science 295 (5563) (2002) 2247.
[4] M.P. Ledbetter, C.W. Crawford, A. Pines, D.E. Wemmer, S. Knappe, J. Kitching, D. Budker, Optical detection of nmr j-spectra at zero magnetic field, J. Magn. Reson. 199 (1) (2009) 25–29.
[5] T. Theis, J.W. Blanchard, M.C. Butler, M.P. Ledbetter, D. Budker, A. Pines, Chemical analysis using j-coupling multiplets in zero-field nmr, Chem. Phys. Lett. 580 (2013) 160–165.
[6] B. Sarah, H. Michael, M. Michael, M. Whittier, W. Travis, M. Michael, C. Kevin, K. Kyle, S. Jeffry, C. John, Measurements of t1 relaxation in ex vivo prostate tissue at 132 μT, Magn. Reson. Med. 67 (4) (2012) 1138–1145.
[7] M. Mossle, S.-I. Han, W.R. Myers, S.-K. Lee, N. Kelso, M. Hatridge, A. Pines, J. Clarke, Squid-detected microtesla mri in the presence of metal, J. Magn. Reson. 179 (1) (2006) 146–151.
[8] K. Kim, S.-J. Lee, C.S. Kang, S.-M. Hwang, Y.-H. Lee, K.-K. Yu, Toward a brain functional connectivity mapping modality by simultaneous imaging of coherent brainwaves, NeuroImage 91 (2014) 63–69.
[9] R. Körber, J.-H. Storm, H. Seton, J.P. Mäkelä, R. Paetau, L. Parkkonen, C. Pfeiffer, B. Riaz, J.F. Schneiderman, H. Dong, et al., Squids in biomagnetism: a roadmap towards improved healthcare, Supercond. Sci. Technol. 29 (11) (2016) 113001.
[10] W.C. Griffith, M.D. Swallows, T.H. Loftus, M.V. Romalis, B.R. Heckel, E.N. Fortson, Improved limit on the permanent electric dipole moment of ^{199}Hg, Phys. Rev. Lett. 102 (10) (2009) 101601.
[11] Y.S. Greenberg, Application of superconducting quantum interference devices to nuclear magnetic resonance, Rev. Modern Phys. 70 (1) (1998) 175.
[12] R. McDermott, S. Lee, B.t. Haken, A.H. Trabesinger, A. Pines, J. Clarke, Microtesla mri with a superconducting quantum interference device, Proc. Natl. Acad. Sci. U.S.A. 101 (21) (2004) 7857.
[13] I.K. Kominis, T.W. Kornack, J.C. Allred, M.V. Romalis, A subfemtotesla multichannel atomic magnetometer, Nature 422 (2003) 596.
[14] D. Budker, M. Romalis, Optical magnetometry, Nat. Phys. 3 (2007) 227.
[15] S.-M. Hwang, K. Kim, C. Seok Kang, S.-J. Lee, Y.-H. Lee, Effective cancellation of residual magnetic interference induced from a shielded environment for precision magnetic measurements, Appl. Phys. Lett. 99 (13) (2011) 132506.
[16] J.O. Nieminen, P.T. Vesanen, K.C. Zevenhoven, J. Dabek, J. Hassel, J. Luomahaara, J.S. Penttilä, R.J. Ilmoniemi, Avoiding eddy-current problems in ultra-low-field mri with self-shielded polarizing coils, J. Magn. Reson. 212 (1) (2011) 154–160.
[17] K.C.J. Zevenhoven, S. Busch, M. Hatridge, F. isjen, R.J. Ilmoniemi, J. Clarke, Conductive shield for ultra-low-field magnetic resonance imaging: theory and measurements of eddy currents, J. Appl. Phys. 115 (10) (2014) 103902, https://doi.org/10.1063/1.4867220.
[18] J.-H. Storm, D. Drung, M. Burghoff, R. Körber, A modular, extendible and field-tolerant multichannel vector magnetometer based on current sensor squids, Supercond. Sci. Technol. 29 (9) (2016) 094001.
[19] S.-J. Lee, J.H. Shim, K. Kim, K.K. Yu, S.-M. Hwang, Dynamic nuclear polarization in the hyperfine-field-dominant region, J. Magn. Reson. 255 (2015) 114–121.
[20] V.S. Zotev, T. Owens, A.N. Matlashov, I.M. Savukov, J.J. Gomez, M.A. Espy, Microtesla mri with dynamic nuclear polarization, J. Magn. Reson. 207 (1) (2010) 78–88.
[21] D.J. Lurie, D.M. Bussell, L.H. Bell, J.R. Mallard, Proton-electron double magnetic resonance imaging of free radical solutions, J. Magn. Reson. 76 (1988) 366–370.
[22] J.-B. Hoevener, N. Schwaderlapp, T. Lickert, S.B. Duckett, R.E. Mewis, L.A.R. Highton, S.M. Kenny, G.G.R. Green, D. Leibfritz, J.G. Korvink, J. Hennig, D. von Elverfeldt, A hyperpolarized equilibrium for magnetic resonance, Nat. Commun. 4 (2013) 2946.
[23] K. Buckenmaier, M. Rudolph, C. Back, T. Misztal, U. Bommerich, P. Fehling, D. Koelle, R. Kleiner, H.A. Mayer, K. Scheffler, J. Bernarding, M. Plaumann, Squid-based detection of ultra-low-field multinuclear nmr of substances hyperpolarized using signal amplification by reversible exchange, Sci. Rep. 7 (1) (2017) 13431.
[24] C.P. Slichter, Principles of Magnetic Resonance, vol. 1, Springer Science & Business Media, 2013.
[25] M.C. Krishna, S. English, K. Yamada, J. Yoo, R. Murugesan, N. Devasahayam, J.A. Cook, K. Golman, J.H. Ardenkjaer-Larsen, S. Subramanian, et al., Overhauser enhanced magnetic resonance imaging for tumor oximetry: coregistration of tumor anatomy and tissue oxygen concentration, Proc. Natl. Acad. Sci. 99 (4) (2002) 2216–2221.

[26] M. Sarracanie, B.D. Armstrong, J. Stockmann, M.S. Rosen, High speed 3d overhauser-enhanced mri using combined b-ssfp and compressed sensing, Magn. Reson. Med. 71 (2) (2014) 735–745.
[27] D.E. Waddington, M. Sarracanie, N. Salameh, F. Herisson, C. Ayata, M.S. Rosen, An overhauser-enhanced-mri platform for dynamic free radical imaging in vivo, NMR Biomed. 31 (5) (2018) e3896.
[28] T. Guiberteau, D. Grucker, Epr spectroscopy by dynamic nuclear polarization in low magnetic field, J. Magn. Reson. Ser. B 110 (1) (1996) 47–54.
[29] S.-J. Lee, J.H. Shim, K. Kim, K.K. Yu, S.-M. Hwang, Magnetic resonance imaging without field cycling at less than earth's magnetic field, Appl. Phys. Lett. 106 (10) (2015) 103702.
[30] T. Liebgott, H. Li, Y. Deng, J.L. Zweier, Proton electron double resonance imaging (pedri) of the isolated beating rat heart, Magn. Reson. Med.: Off. J. Int. Soc. Magn. Reson. Med. 50 (2) (2003) 391–399.
[31] I. Nicholson, D. Lurie, F. Robb, The application of proton-electron double-resonance imaging techniques to proton mobility studies, J. Magn. Reson. Ser. B 104 (3) (1994) 250–255.
[32] J.O. Nieminen, R.J. Ilmoniemi, Solving the problem of concomitant gradients in ultra-low-field mri, J. Magn. Reson. 207 (2) (2010) 213–219.
[33] M. Lustig, D. Donoho, J.M. Pauly, Sparse mri: the application of compressed sensing for rapid mr imaging, Magn. Reson. Med. 58 (6) (2007) 1182–1195.
[34] J.H. Shim, S.-J. Lee, K.-K. Yu, S.-M. Hwang, K. Kim, Strong pulsed excitations using circularly polarized fields for ultra-low field nmr, J. Magn. Reson. 239 (2014) 87–90.
[35] J. Hennig, A. Nauerth, H. Friedburg, Rare imaging: a fast imaging method for clinical mr, Magn. Reson. Med. 3 (6) (1986) 823–833.
[36] H.J. Lee, S.-J. Lee, J.H. Shim, H.S. Moon, K. Kim, In-situ overhauser-enhanced nuclear magnetic resonance at less than 1 μT using an atomic magnetometer, J. Magn. Reson. 300 (2019) 149–152.
[37] R. Ediss, P. Semiconductors, Probing the magnetic field probe, EMC Compl. J. (47).
[38] N.D. Zanche, Birdcage volume coil design, eMagRes.
[39] C. Chin, C.M. Collins, S. Li, B.J. Dardzinski, M.B. Smith, Birdcagebuilder: design of specified geometry birdcage coils with desired current pattern and resonant frequency, Concepts Magn. Reson. 15 (2) (1998) 156–163.
[40] M.C. Leifer, Resonant modes of the birdcage coil, J. Magn. Reson. 124 (1) (1997) 51–60.
[41] F.D. Doty, G. Entzminger Jr, C.D. Hauck, J.P. Staab, Practical aspects of birdcage coils, J. Magn. Reson. 138 (1) (1999) 144–154.
[42] T. Vullo, R.T. Zipagan, R. Pascone, J.P. Whalen, P.T. Cahill, Experimental design and fabrication of birdcage resonators for magnetic resonance imaging, Magn. Reson. Med. 24 (2) (1992) 243–252.